DOI:
10.1097/RLI.0000000000000449

Document Version
Peer reviewed version

Complete manuscript title

Characterization of Small Renal Tumors with MR Elastography: a Feasibility Study

Authors

[1,2]Davide Prezzi, FRCR

[1,3]Radhouene Neji, PhD

[1,2]Christian Kelly-Morland, FRCR

[4]Tim O'Brien, FRCS (Urol)

[4]Ben Challacombe, FRCS (Urol)

[4]Archana Fernando, FRCS (Urol)

[5]Ashish Chandra, FRCPath

[1]Ralph Sinkus, PhD

[1,2]V Goh, FRCR

1. King's College London, School of Biomedical Engineering & Imaging Sciences

   Lambeth Wing, Level 4

   St Thomas' Hospital

   Westminster Bridge Road

   London SE1 7EH

   United Kingdom
2. Guy's and St Thomas' NHS Foundation Trust, Radiology, London, United Kingdom
3. Siemens Healthcare UK, MR Research Collaborations, Frimley, Surrey, United Kingdom
4. Guy's and St Thomas' NHS Foundation Trust, The Urology Centre, London, United Kingdom

5. Guy's and St Thomas' NHS Foundation Trust, Pathology, London, United Kingdom

Corresponding author

Dr Davide Prezzi

School of Biomedical Engineering & Imaging Sciences

Level 4, Lambeth Wing

St Thomas' Hospital

Westminster Bridge Road

London SE1 7EH

United Kingdom

Email: davide.prezzi@kcl.ac.uk

Phone: +44 207 188 5538

Fax: +44 207 188 8447

Funding Information

This work was financially supported by the Royal College of Radiologists through the Clinical Radiology Pump Priming Grant scheme; by the Department of Health via the National Institute for Health Research Comprehensive Biomedical Research Centre award to Guy's and St Thomas' NHS Foundation Trust, in partnership with King's College London and King's College Hospital NHS Foundation Trust; and by the King's College London/University College London Comprehensive Cancer Imaging Centre funded by Cancer Research UK and Engineering and Physical Sciences Research Council, in association with the Medical Research Council and Department of Health. The views expressed in this publication are

those of the authors and not necessarily those of the NHS, the NIHR or the Department of Health.

Short title

MR Elastography of Small Renal Tumors

Acknowledgements

The authors would like to acknowledge the following for their contribution to the successful completion of this study: Mr Sami Jeljeli, Mr James Stirling and the King's College London and Guy's and St Thomas' PET Centre; Dr Hema Verma, consultant radiologist at Guy's and St Thomas' NHS Foundation Trust; and Dr Paul Bassett, statistician at Statsconsultancy Ltd.

Title

Characterization of Small Renal Tumors with MR Elastography: a Feasibility Study

Abstract

Objectives

To explore the feasibility of magnetic resonance elastography (MRE) for characterizing indeterminate small renal tumors (SRT) as part of a multiparametric MR imaging protocol.

Materials and Methods

Following institutional review board approval and informed consent, 21 prospective adults (15 men, median age 55 [range 25-72] years) with SRT were enrolled. Tumors (2 – 5 cm Ø) were imaged using three-directional, gradient echo MRE. Viscoelastic parametric maps (shear wave velocity [*c*] and attenuation [α]) were analyzed by two independent radiologists. Interobserver agreement (Bland-Altman statistics and intraclass correlation coefficients [ICC]) was assessed. Anatomical T2-weighted, dynamic contrast enhanced (DCE) and diffusion sequences completed the acquisition protocol. Imaging parameters were compared between groups (Mann-Whitney U test).

Results

MRE quality was good in 18 cases (mean non-linearity <50%), including one papillary renal cell carcinoma and one metanephric adenoma. A cohort of 5 oncocytomas and 11 clear-cell renal cell carcinomas (ccRCC) was ~~analyzed~~analyzed for statistical differences. MRE viscoelastic parameters were the strongest imaging discriminators: oncocytomas displayed

significantly lower shear velocity *c* (median, 0.77 m/s; interquartile range [IQR], 0.76-0.79) (*P* = 0.007) and higher shear attenuation α (median, 0.087 mm^{-1}; IQR, 0.082-0.087) (*P* = 0.008) than ccRCC (medians, 0.92 m/s and 0.066 mm^{-1}; IQR, 0.84-0.97 and 0.054-0.074 respectively). T2 signal intensity ratio (tumor/renal cortex) was lower in oncocytomas (*P* = 0.02). DCE and diffusion MR parameters overlapped substantially (*P* ≥ 0.1). Oncocytomas displayed a consistent MRE viscoelastic profile, corresponding to data point clustering in a bidimensional scatter plot. MRE ICC were 0.982 for *c* and 0.984 for α, indicating excellent interobserver agreement.

Conclusions

MRE is feasible for SRT characterization; MRE viscoelastic parameters were stronger discriminators between oncocytoma and ccRCC than anatomical, DCE and diffusion MR imaging parameters.

Introduction

Small indeterminate renal tumors (SRT), defined as solid enhancing renal lesions measuring up to 4 cm in diameter, pose a growing challenge to clinical practice (1, 2). Renal cell carcinoma (RCC) accounts for the majority of cases but up to 20% of SRT are benign (3). A recent estimate suggests that ~5600 benign renal tumors undergo surgical resection yearly in the US (4). Image-guided biopsy is performed increasingly to confirm the diagnosis preoperatively (5). Despite providing excellent concordance with surgical histology (6), biopsy is invasive and non-diagnostic in up to 20% of cases (7). A reliable, non-invasive imaging strategy to distinguish benign from malignant SRT would be advantageous, mostly so in patients with multiple comorbidities, and potentially cost effective.

Anatomical and functional MR imaging parameters have shown potential individually to discriminate benign SRT from specific types of RCC (8-16), but their combined diagnostic accuracy has not been investigated in a prospective series to date. Oncocytoma and solid clear cell RCC (ccRCC), respectively the most common benign and malignant indeterminate SRT, share structural and physiological traits (high water content, prominent stroma, dense vascularity) that make their distinction by anatomical and functional MR imaging challenging in many cases (11, 12).

Yet their pathological gross appearance and microscopic structure clearly differ (17, 18): oncocytomas are typically homogenous lesions with frequent central scarring and absent necrosis; microscopically, they are composed of tight cellular nests surrounded by myxoid stroma. Clear cell RCC have a variegated appearance consisting of soft yellow material alternating with areas of hemorrhage, fibrosis, necrosis and cystic degeneration; microscopically, they are composed of lipid- and glycogen-rich cells surrounded by an

extensive capillary network. Oncocytomas have no recognized malignant transformation potential and, once diagnosed, conservative management is safe (19).

MR Elastography (MRE) is an emerging technique that evaluates soft tissue's viscoelastic properties by measuring the shear waves produced by a vibrating mechanical transducer (20). It has been readily incorporated into clinical MR imaging protocols and has been employed successfully in the assessment of hepatic fibrosis (21, 22) and for lesion characterization in the liver, central nervous system and breast (23-26).

We hypothesized that the viscoelastic shear properties of SRT measured by MRE would reflect the underlying tumor composition (e.g. cellular density, extracellular collagen, hemorrhage, necrosis) and architecture (e.g. cellular and connective tissue distribution, vascular size, density and permeability) and therefore differ between histopathological groups. In this study, we aimed to explore the feasibility and diagnostic potential of MRE, performed as part of a multiparametric MR imaging protocol, for characterizing indeterminate small renal tumors (SRT) in patients scheduled for surgery.

Materials and Methods

Participants

This prospective feasibility study was conducted between August 2015 and October 2016, following approval by the national research ethics committees; informed written consent was obtained from all subjects.

Twenty-one patients (15 men and 6 women) with a median age of 55 years (range, 25 to 72 years) and median BMI of 27.0 (range, 19.0 to 29.4), were recruited from a tertiary-care urological clinic. Patients were potentially eligible if under consideration for surgical

resection (partial or total nephrectomy) of an indeterminate solid renal mass measuring ≤5 cm in maximum diameter on cross-sectional imaging. Exclusion criteria were standard contraindications to contrast enhanced MR imaging (e.g. cardiac pacemaker, cochlear implant, significant renal impairment i.e. eGFR <50 mL/min or serum creatinine > 180 µmol/L).

MR Imaging Acquisition

MR imaging was performed on a 3.0 Tesla system (Biograph mMR, Siemens Healthcare GmbH, Erlangen, Germany). ~~It~~The protocol included MRE, anatomical T1 and T2 weighted sequences, dynamic contrast enhanced (DCE) MRI and diffusion-weighted imaging. Patients lied supine (head first) in the scanner and fasted for 4 hours before imaging.

MRE Acquisition

Mechanical vibrations were generated at a frequency of 30 Hz and at 70% of the maximum power by a remote loudspeaker (Resoundant®) and transmitted via compressed air to a disc-shaped passive transducer applied over the patient's flank of interest (mid-axillary line, held in place by an elastic band). A frequency of 30 Hz was selected as a compromise between resolution and efficient wave penetration in the retroperitoneum. MRE was based upon a prototype 2D multi-slice interleaved gradient echo sequence synchronized with the transducer's vibrations (27): repetition time, 11.11 ms (3 shots with a vibration frequency of 30Hz, corresponding to a period of 33.33 ms); echo time, 7.38 ms; motion encoding gradient amplitude, 30 mT/m; GRAPPA parallel imaging acceleration factor, 2; FOV, 265 x 385 mm. Four acquisitions in consecutive expiratory breath holds of 17 s (corresponding to 3 motion-encoding directions and one reference measurement without motion encoding) provided

MRE data within 6 consecutive slices of 128 x 88 pixels at 3 mm isotropic resolution and 4 wave phase offsets. Measurements were performed at mid-tumor level and repeated in 1 or 2 normal portions of the same kidney (standardized to either upper pole, mid-kidney or lower pole), in order to obtain reference measurements from healthy renal parenchyma. Each MRE measurement had an approximate duration of 2 minutes.

MRE Reconstruction

MRE reconstruction used firstly the application of the curl operator for removal of the compressional component, secondly a direct inversion of the Helmholtz equation (28). Parametric maps of shear wave velocity (*c*), a measure of tissue elasticity, and attenuation (α), a measure of viscosity, were generated offline using dedicated in-house software, validated previously (28-30).

Data post-processing was performed by a physicist with over 20 years of experience in MRE. Tumor data analysis was performed independently by two board-certified radiologists with over 7 years of experience in abdominal MR imaging (MRE observer 1 and 2), blinded to histopathology results. Normal kidney measurements were performed by a single radiologist (MRE observer 1).

Free-hand regions of interest (ROI) were drawn around each tumor and around normal renal parenchyma (including both cortex and medulla, aiming to match the size of tumor ROI) on the two contiguous central slices of magnitude images, with reference to the available anatomical sequences, and ~~transposed automatically via geometrical mapping~~copied onto the ~~two contiguous central slices of~~ parametric maps. The mean and standard deviation of the quantified parameters were recorded for each case.

MRE Quality Assessment

Parametric maps of data 'non-linearity', displaying the percentage deviation of the phase signal from a perfect sinusoidal modulation, were assessed by both readers for each MRE measurement, using the same ROI as previously, and the mean 'non-linearity' percentage documented. A threshold of <50% mean 'non-linearity' was defined as acceptable data quality.

Anatomical and Functional MR Imaging

Anatomical imaging included a T2-weighted half-Fourier single-shot turbo spin echo sequence (HASTE) (TR, 1000 msec; TE, 97 msec; FA, 135°; NEX, 1; GRAPPA parallel imaging acceleration factor, 2; FOV, 384 x 250 mm; pixel size, 1.5 x 1.2 x 3.0 mm) acquired in the axial plane.

Dynamic contrast-enhanced (DCE) MR imaging was based on a 3D T1-weighted axial volumetric interpolated spoiled gradient echo sequence (VIBE) (TR, 4.62 msec; TE, 1.72 msec; FA, 18°; number of signals acquired, 1; parallel imaging acceleration factor, 2; FOV, 300 x 244 mm; pixel size, 1.8 x 1.3 x 4.0 mm). 0.1 mmol/kg of gadolinium contrast agent was administered intravenously (Gadovist®, Bayer) at a rate of 4 mL/sec using a power injector, followed by a 20 mL saline chaser; 30 volumes were acquired post contrast injection over 3 minutes, resulting in a temporal resolution of 6.4 sec. The dynamic acquisition was preceded by a T1 calibration sequence with the same parameters except a flip angle of 3°.

Diffusion-weighted imaging consisted of free-breathing single-shot echo-planar imaging in the axial plane with *b* values of 50, 500 and 800 mm^2/sec. Imaging parameters were as follows: TR, 6100 msec; TE, 62 msec; NEX, 5; parallel imaging acceleration factor, 2; FOV, 380 x 285 mm; pixel size 3.7 x 3.0 x 4.0 mm.

Anatomical and functional sequences were post processed and analyzed offline on a commercial platform (Multimodality Workplace, Siemens). All quantitative measurements were performed by a single radiologist ~~(DP)~~(MRE observer 1), blinded to histopathology. Freehand ROI were drawn on each slice displaying the lesion of interest; volumetric means were analyzed. T2 signal intensity (SI) ratio was calculated as the % ratio of tumor over renal cortex on the T2 HASTE sequence (8).

DCE MR imaging parametric maps, including transfer coefficient (K^{trans}), rate constant (k_{ep}), extracellular-extravascular space fractional volume (v_e) and initial area under the concentration curve for the first 60 seconds ($iAUC_{60}$), were generated on dedicated software (Tissue 4D; Siemens); nonrigid motion correction and registration to the calibration sequence were applied to the dynamic acquisition; quantification was based on the two-compartment Tofts model (31), using a pre-set population averaged arterial input function. Apparent diffusion coefficient (ADC) maps were generated by fitting a mono-exponential function to all *b* values.

Statistics

All statistical analyses were performed using IBM SPSS version 23.0 software. Continuous variables were regarded as non-normally distributed and expressed as medians and interquartile range. Measurements were compared between the two main histological groups using the non-parametric Mann-Whitney U test. Mean interobserver MRE values were used in the analysis. $P < .05$ was considered indicative of a significant difference. Interobserver agreement was assessed using Bland-Altman (BA) statistics and intraclass correlation coefficients (ICC). MRE within-subject variability in healthy renal parenchyma

was expressed in terms of mean differences and coefficients of variance (CV). Missing data were omitted from the analysis.

Results

One patient did not complete imaging due to claustrophobia, leaving 20 complete imaging datasets including MRE. Surgical histopathology became available for 19 patients and revealed 4 renal oncocytomas, 12 ccRCC (1, Fuhrman grade 3; 8, grade 2; 3, grade 1), 2 papillary RCC and 1 metanephric adenoma. One further case of renal oncocytoma was diagnosed from image-guided biopsy and surgery was deferred. Tumor diameters ranged between 2.2 and 5.0 cm. All imaging sessions were completed in less than 60 minutes.

MRE of Tumors

Two tumor MRE datasets were excluded for insufficient quality, secondary to poor patient compliance with breath hold instructions and consequent high data non-linearity (>50%), leaving a cohort of 11 clear cell renal cell carcinomas (ccRCC) and 5 oncocytomas for statistical analysis.

Shear wave velocity *c* was significantly lower in oncocytomas (median, 0.77 m/s; interquartile range (IQR), 0.76-0.79) than in ccRCC (median, 0.92 m/s; IQR, 0.84-0.97) (P = 0.007). Shear wave attenuation α was significantly higher in oncocytomas (median, 0.087 mm^{-1}; IQR, 0.082-0.087) than in ccRCC (median, 0.066 mm^{-1}; IQR, 0.054-0.074) (P = 0.008). Complete results, including case-by-case mean values and standard deviations, are reported in Table 1. Pictorial examples are shown in Figure 1. Oncocytomas displayed a relatively narrow range of values (*c* range, 0.71-0.83 m/s; α range, 0.082-0.093 mm^{-1}), corresponding

to data point clustering in a bidimensional scatter plot (Figure 2). ccRCC had wider ranges (*c* range, 0.79-1.11 m/s; α range, 0.046-0.083 mm^{-1}), resulting in a broader data point scatter. The only papillary RCC imaged with sufficient data quality showed relatively low *c* (0.77 m/s, coinciding with the median value of oncocytomas) and low α (0.064 mm^{-1}, close to the median of ccRCC). Metanephric adenoma displayed relatively low *c* (0.78 m/s) and intermediate α (0.079 mm^{-1}).

MRE Interobserver Agreement

Mean ROI size was 226 ± 109 pixels for observer 1 and 196 ± 102 pixels for observer 2. Mean differences in tumors were 0.002 m/s [*c*] and -0.0005 mm^{-1} [α]. Bland-Altman limits of agreement were the mean differences as previously ± 0.055 m/s [*c*] and ± 0.0077 mm^{-1} [α] respectively (Figure 3). ICC (95% confidence intervals) were 0.982 (0.953-0.993) [*c*] and 0.984 (0.957-0.994) [α], indicating excellent agreement.

MRE of Normal Kidney

A total of 31 MRE measurements of acceptable quality were performed in normal portions of the tumor-containing kidneys. Mean shear velocity *c* in the renal parenchyma was 0.89 ± 0.10 m/s; mean shear attenuation α was 0.072 ± 0.012 mm^{-1}.

Two separate measurements in different portions of the same kidney were acquired in a subset of 10 patients. Mean within-subject differences were 0.10 ± 0.05 m/s for *c* and 0.014 ± 0.010 mm^{-1} for α, corresponding to CV of 7.81 ± 4.61% and 14.24 ± 10.72% respectively.

Anatomical and Functional MR Imaging of Tumors

Tumor parametric values are reported in Table 1. Oncocytomas had significantly lower T2 SI ratio (median, 93%; interquartile range, 89-93%) than ccRCC (median, 120%; interquartile

range, 103-128%) (*P* = 0.020). No statistically significant difference between the two histological groups was observed among functional MR imaging parameters. Oncocytomas appeared on average more vascular on DCE MR imaging, with higher $iAUC_{60}$ (median, 59 mmol; *P* = 0.100), K^{trans} (median, 0.24 min^{-1}; *P* = 0.126), k_{ep} (median, 0.66 min^{-1}; *P* = 0.193) and lower v_e (median, 0.30 mL/100 mL; *P* = 0.692). ADC varied considerably within both groups, being on average lower in oncocytomas (median, 1363 x 10^{-6} mm^2/s) (*P* = 0.193). Both papillary RCC displayed markedly restricted diffusion (ADC = 839 and 959 x 10^{-6} mm^2/s) and low T2 SI ratios (74% and 55%), in line with the existing literature (32, 33). The metanephric adenoma showed relatively low T2 SI ratio (58%) and contrast enhancement ($iAUC_{60}$ = 19 mmol)(34). Only partial data point clustering was obtained by plotting T2 SI ratio against ADC (Figure 2B). No clustering was observed by plotting DCE MR K^{trans} against v_e (Figure 2C).

Among qualitative anatomical tumor features, a T2 pseudocapsule was present in 2 out of 5 oncocytomas and 10 out of 12 ccRCC; central T2 hyperintensity was observed in 3 oncocytomas and 1 ccRCC; and signal drop on opposed-phase chemical shift MRI in no oncocytoma and 7 ccRCC.

Discussion

Our study shows that MRE is feasible, as part of a multiparametric MR protocol, for the characterization of small indeterminate renal tumors and represents a promising technique for distinguishing benign oncocytoma from malignant clear cell carcinoma. MRE shear velocity *c* and shear attenuation α were the strongest imaging discriminators between oncocytoma and ccRCC in this initial prospective cohort of 20 patients.

Identifying renal oncocytoma among indeterminate SRT is problematic based on imaging alone, even using multiparametric MR, as highlighted by current literature. Among anatomical MR imaging parameters, T2 signal intensity has been shown to be higher in ccRCC than in oncocytoma and chromophobe RCC, but the overlap is substantial (35, 36). T2 SI ratio was in fact the third best discriminator between oncocytoma and ccRCC in our study. The presence of a central area of T2 signal hyperintensity, compatible with necrosis or fibrosis, can be observed in both oncocytoma and RCC (8, 9). Chemical shift MR, combined with delayed contrast enhanced imaging, has been found to have a high negative predictive value for oncocytoma (97%), by revealing the typical absence of fat and the presence of enhancing central fibrosis: these findings, however, have yet to be validated prospectively (10). A T2 hypointense pseudocapsule, commonly observed in SRT, is also nonspecific (16). Diffusion and contrast enhancement characteristics can discriminate between types of RCC but again are known to overlap between oncocytoma and ccRCC (32, 37); this was the case in our cohort, where DCE MR $iAUC_{60}$ was the strongest functional discriminator (P = .10), being higher in oncocytomas. Taouli et al. previously found significantly lower ADC values in solid ccRCC than in oncocytomas, but only after excluding Bosniak 4 ccRCC (i.e. solid masses with a large cystic or a necrotic component), potentially indistinguishable from oncocytoma in our experience (11). No significant signal intensity change was observed by Vargas et al. on contrast-enhanced MR between ccRCC and oncocytoma in any phase of enhancement (12).

To our knowledge, this study is the first to investigate the viscoelastic properties of SRT using MRE. Published reports employing semiquantitative (strain) or quantitative (shear-wave) ultrasound elastography techniques for differentiating benign from malignant renal

tumors found RCC to be stiffer than benign lesions such as angiomyolipoma; no oncocytomas were included, however (38-40).

Our results support the hypothesis that differences in tumor composition and structural architecture, clearly distinguishable on histopathology between oncocytoma and RCC, are reflected by MRE viscoelastic shear properties. Oncocytomas showed lower shear wave velocity, corresponding to lower stiffness (storage modulus), and higher shear attenuation (loss modulus), corresponding to higher viscosity, than ccRCC. This is in line with the evidence that malignancy increases stiffness through collagen deposition in the extracellular matrix and raised interstitial pressure levels from the altered vasculature (41, 42). Lower MRE stiffness values in benign versus malignant tumors have been documented in the breast and in the liver (23, 26, 43, 44).

Few studies to date have assessed tumors in terms of shear wave attenuation. The loss modulus was found to be significantly higher in hepatocellular carcinoma than in benign liver tumors (hemangioma, focal nodular hyperplasia, adenoma) by Garteiser et al. (23), contrasting with our results. We speculate that the higher shear wave attenuation values measured in oncocytoma might reflect a high density of capillaries with normal endothelium, resulting in efficient energy dispersion in the form of heat and contrasting with the disorganized vasculature and leaky endothelium typical of renal carcinomas.

Propagating waves could be appreciated on phase images in all MRE acquisitions. Two out of 20 datasets were excluded for insufficient quality, defined as nonlinearity >50%. In one case (ccRCC-07, Table 1), respiratory motion was identified as the main causative factor from the presence of blurred renal contours on the magnitude images. In the second case (papRCC-02) (Figure 4), wave penetration inside the lesion was ~~poor~~inconsistent with an incompressible material (as if detached from the surrounding tissue) ~~inside the lesion~~

despite good penetration in the adjacent kidney; this was a hemorrhagic papillary RCC, showing marked signal hypointensity on T2 HASTE. Interestingly, one of the main causes identified by Wagner et al. for technical MRE failure in the liver at 3T (45) was hepatic iron deposition, causing shortening of T2* relaxation. Intratumoral hemorrhage is frequent in papillary RCC, but is not known to occur in oncocytoma; low ADC values are the dominant MR feature of papillary RCC and in our experience it seems unlikely that MRE will be the main determinant for papillary RCC characterization.

The average level of phase signal nonlinearity was ~30% throughout MRE acquisitions, corresponding to our previous clinical experience using the Resoundant® system in the upper abdomen. New bespoke transducers, based upon a gravitational concept for generating shear waves (46), are expected to lower this level and thereby increase the reproducibility of viscoelastic parameters. MRE interobserver limits of agreement (mean difference ± 0.055 m/s [*c*] and ± 0.0077 mm^{-1} [α]) were deemed within acceptable limits and appear unlikely to affect the significance of between-group differences.

Of the two MRE parameters, *c* was less dispersed around the mean value in tumor ROI: SD ranged between 0.11 and 0.30 m/s (Table 1), corresponding to a CV of ~14-28%. MRE *c* SD were noticeably lower in oncocytomas than ccRCC; this was not the case for MRE α or anatomical/functional MR imaging parameters. Within-subject variability in healthy renal parenchyma was 7.81 ± 4.61% for *c* and 14.24 ± 10.72% for α. Similarly, Rouviere et al. (47) found a mean shear wave velocity variation of 6% (range, 2 - 16%) between two independent measurements in the kidney of young healthy adults at 45 Hz, also using a gradient echo sequence at 1.5 T. Although not directly comparable, a recent meta-analysis on MRE repeatability in the liver identified a measured change in hepatic stiffness of 22% or greater as a reliable true change (95% confidence) (48).

Despite our promising results, our study does have limitations: the small study cohort reflects its exploratory nature and does not allow us to draw definitive conclusions on the diagnostic accuracy of MR imaging parameters. Prospective recruitment of consecutive patients from a single tertiary clinic meant that only the most common SRT histologies were captured. The decision to include tumors ≤ 5 cm in diameter (contrasting with the conventional definition of small renal mass, ≤ 4 cm) was made to facilitate patient recruitment. Less common histologies such as chromophobe RCC, often morphologically indistinguishable from oncocytoma (36), and fat poor AML (35) were not part of our prospective cohort.

In conclusion, MRE is feasible and practicable for the characterization of small indeterminate renal tumors as part of a multiparametric MR protocol. This feasibility study highlights the diagnostic potential of MRE for distinguishing renal oncocytoma from ccRCC, strengthening the case for confirmation of these results in a powered diagnostic accuracy study.

References

1. Hollingsworth JM, Miller DC, Daignault S, Hollenbeck BK. Rising incidence of small renal masses: a need to reassess treatment effect. J Natl Cancer Inst. 2006;98(18):1331-4.

2. Gill IS, Aron M, Gervais DA, Jewett MA. Clinical practice. Small renal mass. N Engl J Med. 2010;362(7):624-34.

3. Frank I, Blute ML, Cheville JC, Lohse CM, Weaver AL, Zincke H. Solid renal tumors: an analysis of pathological features related to tumor size. J Urol. 2003;170(6 Pt 1):2217-20.

4. Johnson DC, Vukina J, Smith AB, et al. Preoperatively misclassified, surgically removed benign renal masses: a systematic review of surgical series and United States population level burden estimate. J Urol. 2015;193(1):30-5.

5. Finelli A, Ismaila N, Russo P. Management of Small Renal Masses: American Society of Clinical Oncology Clinical Practice Guideline Summary. J Oncol Pract. 2017:JOP2016019620.

6. Marconi L, Dabestani S, Lam TB, et al. Systematic Review and Meta-analysis of Diagnostic Accuracy of Percutaneous Renal Tumour Biopsy. Eur Urol. 2016;69(4):660-73.

7. Leveridge MJ, Finelli A, Kachura JR, et al. Outcomes of small renal mass needle core biopsy, nondiagnostic percutaneous biopsy, and the role of repeat biopsy. Eur Urol. 2011;60(3):578-84.

8. Rosenkrantz AB, Hindman N, Fitzgerald EF, Niver BE, Melamed J, Babb JS. MRI features of renal oncocytoma and chromophobe renal cell carcinoma. AJR Am J Roentgenol. 2010;195(6):W421-7.

9. Ball DS, Friedman AC, Hartman DS, Radecki PD, Caroline DF. Scar sign of renal oncocytoma: magnetic resonance imaging appearance and lack of specificity. Urol Radiol. 1986;8(1):46-8.

10. Cornelis F, Lasserre AS, Tourdias T, et al. Combined late gadolinium-enhanced and double-echo chemical-shift MRI help to differentiate renal oncocytomas with high central T2 signal intensity from renal cell carcinomas. AJR Am J Roentgenol. 2013;200(4):830-8.

11. Taouli B, Thakur RK, Mannelli L, et al. Renal lesions: characterization with diffusion-weighted imaging versus contrast-enhanced MR imaging. Radiology. 2009;251(2):398-407.

12. Vargas HA, Chaim J, Lefkowitz RA, et al. Renal cortical tumors: use of multiphasic contrast-enhanced MR imaging to differentiate benign and malignant histologic subtypes. Radiology. 2012;264(3):779-88.

13. Kang SK, Zhang A, Pandharipande PV, Chandarana H, Braithwaite RS, Littenberg B. DWI for Renal Mass Characterization: Systematic Review and Meta-Analysis of Diagnostic Test Performance. AJR Am J Roentgenol. 2015;205(2):317-24.

14. Sasiwimonphan K, Takahashi N, Leibovich BC, Carter RE, Atwell TD, Kawashima A. Small (<4 cm) renal mass: differentiation of angiomyolipoma without visible fat from renal cell carcinoma utilizing MR imaging. Radiology. 2012;263(1):160-8.

15. Verma SK, Mitchell DG, Yang R, et al. Exophytic renal masses: angular interface with renal parenchyma for distinguishing benign from malignant lesions at MR imaging. Radiology. 2010;255(2):501-7.

16. Roy C, El Ghali S, Buy X, et al. Significance of the pseudocapsule on MRI of renal neoplasms and its potential application for local staging: a retrospective study. AJR Am J Roentgenol. 2005;184(1):113-20.

17. Amin MB, Crotty TB, Tickoo SK, Farrow GM. Renal oncocytoma: a reappraisal of morphologic features with clinicopathologic findings in 80 cases. Am J Surg Pathol. 1997;21(1):1-12.

18. Andeen N. Kidney tumor - cysts, children, adult benign. Adult renal cell carcinoma. Clear cell renal cell carcinoma. http://www.pathologyoutlines.com/topic/kidneytumormalignantrccclear.html. Published January 30, 2017. Accessed September 4, 2017.

19. Romis L, Cindolo L, Patard JJ, et al. Frequency, clinical presentation and evolution of renal oncocytomas: multicentric experience from a European database. Eur Urol. 2004;45(1):53-7; discussion 7.

20. Muthupillai R, Lomas DJ, Rossman PJ, Greenleaf JF, Manduca A, Ehman RL. Magnetic resonance elastography by direct visualization of propagating acoustic strain waves. Science. 1995;269(5232):1854-7.

21. Bohte AE, Garteiser P, De Niet A, et al. MR elastography of the liver: defining thresholds for detecting viscoelastic changes. Radiology. 2013;269(3):768-76.

22. Singh S, Venkatesh SK, Wang Z, et al. Diagnostic performance of magnetic resonance elastography in staging liver fibrosis: a systematic review and meta-analysis of individual participant data. Clin Gastroenterol Hepatol. 2015;13(3):440-51.e6.

23. Garteiser P, Doblas S, Daire JL, et al. MR elastography of liver tumours: value of viscoelastic properties for tumour characterisation. Eur Radiol. 2012;22(10):2169-77.

24. Hughes JD, Fattahi N, Van Gompel J, et al. Higher-Resolution Magnetic Resonance Elastography in Meningiomas to Determine Intratumoral Consistency. Neurosurgery. 2015;77(4):653-8; discussion 8-9.

25. Hughes JD, Fattahi N, Van Gompel J, Arani A, Ehman R, Huston J. Magnetic resonance elastography detects tumoral consistency in pituitary macroadenomas. Pituitary. 2016;19(3):286-92.

26. Sinkus R, Tanter M, Xydeas T, Catheline S, Bercoff J, Fink M. Viscoelastic shear properties of in vivo breast lesions measured by MR elastography. Magn Reson Imaging. 2005;23(2):159-65.

27. Garteiser P, Sahebjavaher RS, Ter Beek LC, et al. Rapid acquisition of multifrequency, multislice and multidirectional MR elastography data with a fractionally encoded gradient echo sequence. NMR Biomed. 2013;26(10):1326-35.

28. Sinkus R, Siegmann K, Xydeas T, Tanter M, Claussen C, Fink M. MR elastography of breast lesions: understanding the solid/liquid duality can improve the specificity of contrast-enhanced MR mammography. Magn Reson Med. 2007;58(6):1135-44.

29. Green MA, Bilston LE, Sinkus R. In vivo brain viscoelastic properties measured by magnetic resonance elastography. NMR Biomed. 2008;21(7):755-64.

30. Etchell E, Jugé L, Hatt A, Sinkus R, Bilston LE. Liver Stiffness Values Are Lower in Pediatric Subjects than in Adults and Increase with Age: A Multifrequency MR Elastography Study. Radiology. 2017;283(1):222-30.

31. Tofts PS, Kermode AG. Measurement of the blood-brain barrier permeability and leakage space using dynamic MR imaging. 1. Fundamental concepts. Magn Reson Med. 1991;17(2):357-67.

32. Wang H, Cheng L, Zhang X, et al. Renal cell carcinoma: diffusion-weighted MR imaging for subtype differentiation at 3.0 T. Radiology. 2010;257(1):135-43.

33. Oliva MR, Glickman JN, Zou KH, et al. Renal cell carcinoma: t1 and t2 signal intensity characteristics of papillary and clear cell types correlated with pathology. AJR Am J Roentgenol. 2009;192(6):1524-30.

34. Yan J, Cheng JL, Li CF, et al. The findings of CT and MRI in patients with metanephric adenoma. Diagn Pathol. 2016;11(1):104.

35. Schieda N, Dilauro M, Moosavi B, et al. MRI evaluation of small (<4cm) solid renal masses: multivariate modeling improves diagnostic accuracy for angiomyolipoma without visible fat compared to univariate analysis. Eur Radiol. 2016;26(7):2242-51.

36. Galmiche C, Bernhard JC, Yacoub M, Ravaud A, Grenier N, Cornelis F. Is Multiparametric MRI Useful for Differentiating Oncocytomas From Chromophobe Renal Cell Carcinomas? AJR Am J Roentgenol. 2017;208(2):343-50.

37. Wang HY, Su ZH, Xu X, et al. Dynamic Contrast-enhanced MRI in Renal Tumors: Common Subtype Differentiation using Pharmacokinetics. Sci Rep. 2017;7(1):3117.

38. Tan S, Özcan MF, Tezcan F, et al. Real-time elastography for distinguishing angiomyolipoma from renal cell carcinoma: preliminary observations. AJR Am J Roentgenol. 2013;200(4):W369-75.

39. Göya C, Daggulli M, Hamidi C, et al. The role of quantitative measurement by acoustic radiation force impulse imaging in differentiating benign renal lesions from malignant renal tumours. Radiol Med. 2015;120(3):296-303.

40. Lu Q, Wen JX, Huang BJ, Xue LY, Wang WP. Virtual Touch quantification using acoustic radiation force impulse (ARFI) technology for the evaluation of focal solid renal lesions: preliminary findings. Clin Radiol. 2015;70(12):1376-81.

41. Dvorak HF. Tumors: wounds that do not heal. Similarities between tumor stroma generation and wound healing. N Engl J Med. 1986;315(26):1650-9.

42. Heldin CH, Rubin K, Pietras K, Ostman A. High interstitial fluid pressure - an obstacle in cancer therapy. Nat Rev Cancer. 2004;4(10):806-13.

43. Hennedige TP, Hallinan JT, Leung FP, et al. Comparison of magnetic resonance elastography and diffusion-weighted imaging for differentiating benign and malignant liver lesions. Eur Radiol. 2016;26(2):398-406.

44. McKnight AL, Kugel JL, Rossman PJ, Manduca A, Hartmann LC, Ehman RL. MR elastography of breast cancer: preliminary results. AJR Am J Roentgenol. 2002;178(6):1411-7.

45. Wagner M, Corcuera-Solano I, Lo G, et al. Technical Failure of MR Elastography Examinations of the Liver: Experience from a Large Single-Center Study. Radiology. 2017:160863.

46. Runge J, Hoelzl S, Sudakova J, et al. A novel MR Elastography transducer concept based on a rotational eccentric mass: the gravitational transducer. Conference abstract #1369. ISMRM Annual Meeting 2017, Honolulu, USA.

47. Rouvière O, Souchon R, Pagnoux G, Ménager JM, Chapelon JY. Magnetic resonance elastography of the kidneys: feasibility and reproducibility in young healthy adults. J Magn Reson Imaging. 2011;34(4):880-6.

48. Serai SD, Obuchowski NA, Venkatesh SK, et al. Repeatability of MR Elastography of Liver: A Meta-Analysis. Radiology. 2017:161398.

Tables

Table 1. Results from tumor multiparametric MR imaging, displayed by tumor histology.

Note. Tumor diameters as measured at surgical histopathology. Mean values ± standard deviation. *P* values for between-group comparisons were determined with the Mann-Whitney U test. IQR = interquartile range. - = missing value.

Case #	Diameter (cm)	*c* (m/s)	α (mm^{-1})	$iAUC_{60}$ (mmol)	K^{trans} (min^{-1})	K_{ep} (min^{-1})	V_e (mL/100 mL)	T2 SI RATIO (%)	ADC (10^{-6} x mm^2/s)
RENAL ONCOCYTOMA									
ONCO-1	4.2	0.83 ± 0.16	0.093 ± 0.033	72 ± 34	0.31 ± 0.17	0.99 ± 0.37	0.30 ± 0.14	93 ± 30	1949 ± 338
ONCO-2	5.0	0.79 ± 0.16	0.082 ± 0.035	32 ± 16	0.09 ± 0.05	0.32 ± 0.16	0.28 ± 0.15	86 ± 27	1319 ± 260
ONCO-3	5.0	0.77 ± 0.14	0.082 ± 0.048	80 ± 38	0.41 ± 0.24	1.15 ± 0.58	0.33 ± 0.17	89 ± 24	1348 ± 284
ONCO-4	3.1	0.76 ± 0.11	0.087 ± 0.044	59 ± 22	0.24 ± 0.10	0.62 ± 0.23	0.39 ± 0.14	124 ± 40	1961 ± 315
ONCO-5	4.5	0.71 ± 0.11	0.087 ± 0.042	51 ± 32	0.20 ± 0.13	0.66 ± 0.26	0.29 ± 0.16	93 ± 30	1363 ± 231
Median (IQR)	4.5 (4.2-5.0)	0.77 (0.76-0.79)	0.087 (0.082-0.087)	59 (51-72)	0.24 (0.20-0.31)	0.66 (0.62-0.99)	0.30 (0.29-0.33)	93 (89-93)	1363 (1348-1949)
CLEAR CELL RENAL CELL CARCINOMA									
ccRCC-01	3.3	1.00 ± 0.28	0.060 ± 0.027	29 ± 20	0.11 ± 0.09	0.47 ± 0.30	0.24 ± 0.17	126 ± 40	1760 ± 326
ccRCC-02	3.0	0.79 ± 0.12	0.072 ± 0.054	63 ± 29	0.21 ± 0.10	0.51 ± 0.15	0.40 ± 0.17	106 ± 23	1590 ± 184
ccRCC-03	3.6	0.83 ± 0.16	0.070 ± 0.040	50 ± 43	0.19 ± 0.20	0.41 ± 0.36	0.33 ± 0.30	101 ± 34	1695 ± 365
ccRCC-04	2.8	0.94 ± 0.19	0.066 ± 0.035	55 ± 34	0.22 ± 0.17	0.74 ± 0.46	0.29 ± 0.17	102 ± 31	1722 ± 320
ccRCC-05	2.5	0.84 ± 0.23	0.083 ± 0.045	46 ± 32	0.17 ± 0.13	0.33 ± 0.23	0.45 ± 0.26	141 ± 44	2118 ± 394
ccRCC-06	3.0	0.86 ± 0.18	0.085 ± 0.030	23 ± 22	0.09 ± 0.09	0.63 ± 1.42	0.18 ± 0.17	121 ± 37	1929 ± 303
ccRCC-07	2.7	-	-	62 ± 44	0.24 ± 0.18	0.62 ± 0.38	0.33 ± 0.23	94 ± 32	1433 ± 255

ccRCC-08	3.5	1.11 ± 0.30	0.052 ± 0.032	27 ± 21	0.11 ± 0.09	0.30 ± 0.24	0.38 ± 0.27	152 ± 47	2483 ± 424
ccRCC-09	4.2	0.92 ± 0.24	0.046 ± 0.033	61 ± 31	0.27 ± 0.16	0.71 ± 0.28	0.37 ± 0.20	124 ± 45	1512 ± 460
ccRCC-10	4.0	0.93 ± 0.19	0.032 ± 0.022	47 ± 43	0.19 ± 0.18	0.68 ± 0.56	0.26 ± 0.24	104 ± 35	1795 ± 295
ccRCC-11	3.4	1.00 ± 0.23	0.075 ± 0.050	29 ± 21	0.11 ± 0.09	0.38 ± 0.38	0.30 ± 0.19	120 ± 54	1984 ± 348
ccRCC-12	2.2	0.80 ± 0.14	0.056 ± 0.028	51 ± 19	0.15 ± 0.07	0.30 ± 0.15	0.49 ± 0.22	134 ± 39	1612 ± 155
Median (IQR)	3.2 (2.8-3.5)	0.92 (0.84-0.97)	0.066 (0.054-0.074)	48 (29-57)	0.18 (0.11-0.21)	0.49 (0.36-0.64)	0.33 (0.28-0.39)	120 (103-128)	1741 (1606-1943)
***P* value**	.017	.007	.008	.100	.126	.193	.692	.020	.193
PAPILLARY RENAL CELL CARCINOMA									
papRCC-01	3.7	0.77 ± 0.10	0.062 ± 0.029	30 ± 20	0.11 ± 0.10	0.68 ± 0.40	0.17 ± 0.14	74 ± 17	839 ± 218
papRCC-02	4.1	-	-	15 ± 19	0.06 ± 0.04	0.50 ± 0.55	0.16 ± 0.10	55 ± 35	959 ± 602
METANEPHRIC ADENOMA									
MA-01	5.0	0.78 ± 0.15	0.079 ± 0.033	19 ± 12	0.11 ± 0.07	0.17 ± 0.20	0.37 ± 0.21	58 ± 14	1222 ± 339

Figure Captions

Figure 1. **A**. Fuhrman grade 2, 2.7 cm ccRCC in a 67-year-old man. **B**. 3.1 cm renal oncocytoma in a 51-year-old man. Axial MR imaging sections. Anatomical T2 HASTE (top left), ADC map (middle), cortico-medullary phase contrast-enhanced T1 VIBE (top right), MRE magnitude image (bottom left), MRE *c* (middle) and MRE α (bottom right) parametric maps. Morphological and functional imaging features are indistinguishable between the two histologies. Oncocytoma displays relatively lower shear velocity *c* and higher shear attenuation α. Tumors are contoured in red on MRE magnitude images and parametric maps. The adjacent kidney is contoured in pink and can be clearly distinguished from the surrounding structures on MRE shear velocity maps.

Figure 2. Bidimensional scatter plots of tumor MR imaging parameters. Oncocytomas display a consistent MRE viscoelastic profile, corresponding to data point clustering (A). Only partial clustering is obtained by plotting T2 SI ratio against ADC (B). No clustering is observed by plotting DCE MR K^{trans} against v_e (C).

Figure 3. Interobserver agreement. Bland-Altman graphs of MRE *c* (left) and α (right), plotting interobserver differences against their mean. Red dotted lines represent 95% Bland-Altman limits of agreement; blue line represents the mean difference.

Figure 4. Type 1, 4.1 cm papillary RCC in a 66-year-old man: axial MR imaging sections. Anatomical T2 HASTE (left), MRE gradient-echo magnitude image (middle) and MRE non-linearity parametric map (right). Intra-tumoral ~~hemorrhage~~haemorrhage, confirmed at histology, corresponds to low signal intensity in A and B. MRE phase signal shows elevated non-linearity within the tumor (~80%) compared to adjacent renal parenchyma (~35%).

Figure 1A

Click here to download Figure Figure 1a - revised.png

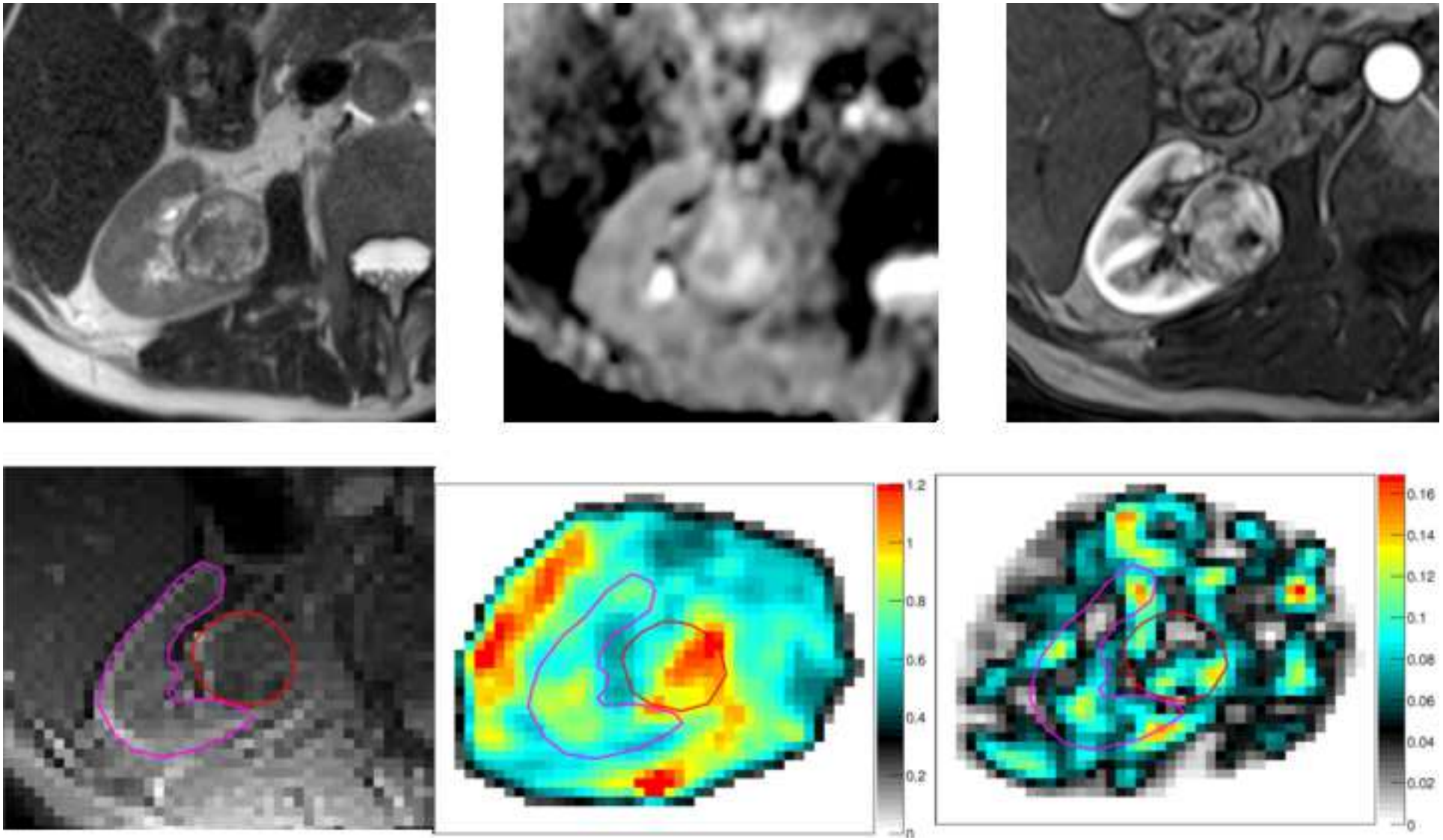

Figure 1B

Click here to download Figure Figure1b - revised.png

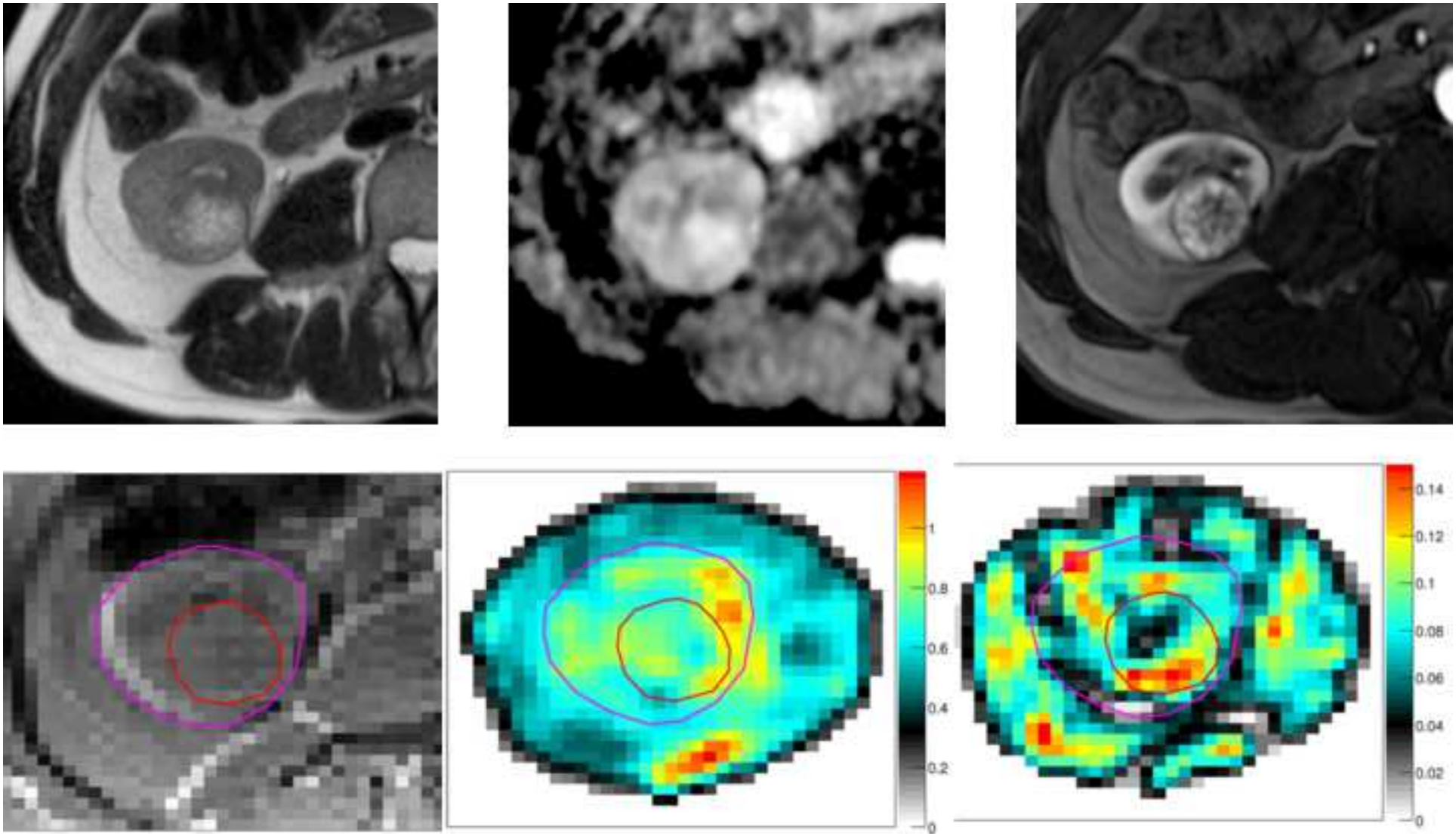

Figure 2

Click here to download Figure Figure 2 - revised.png

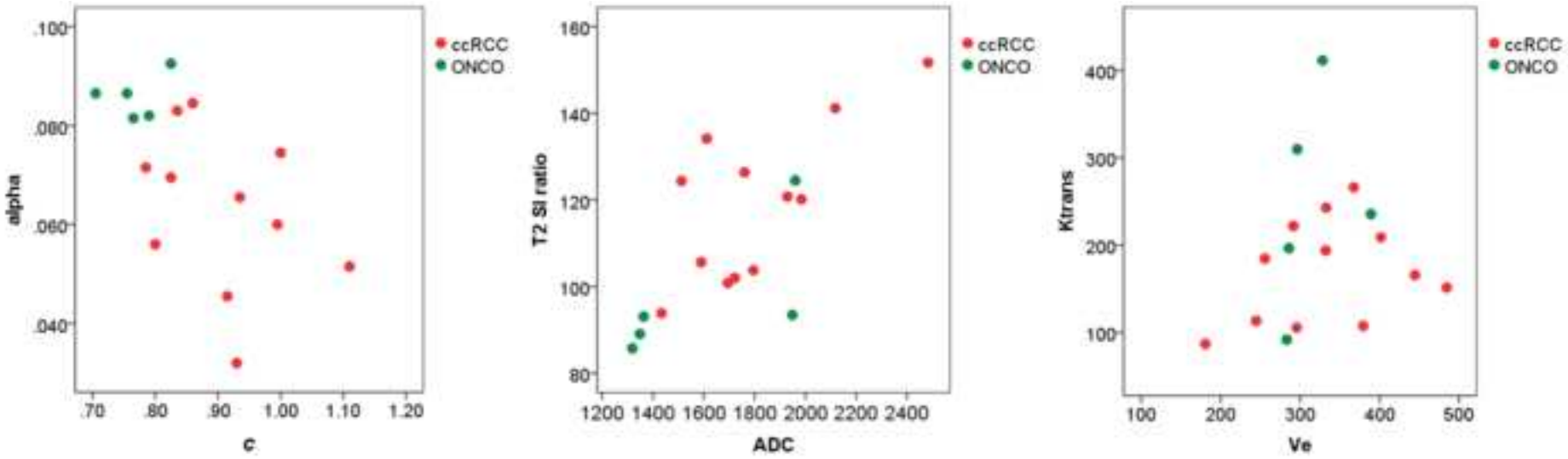

Figure 3

Click here to download Figure Figure 3.png

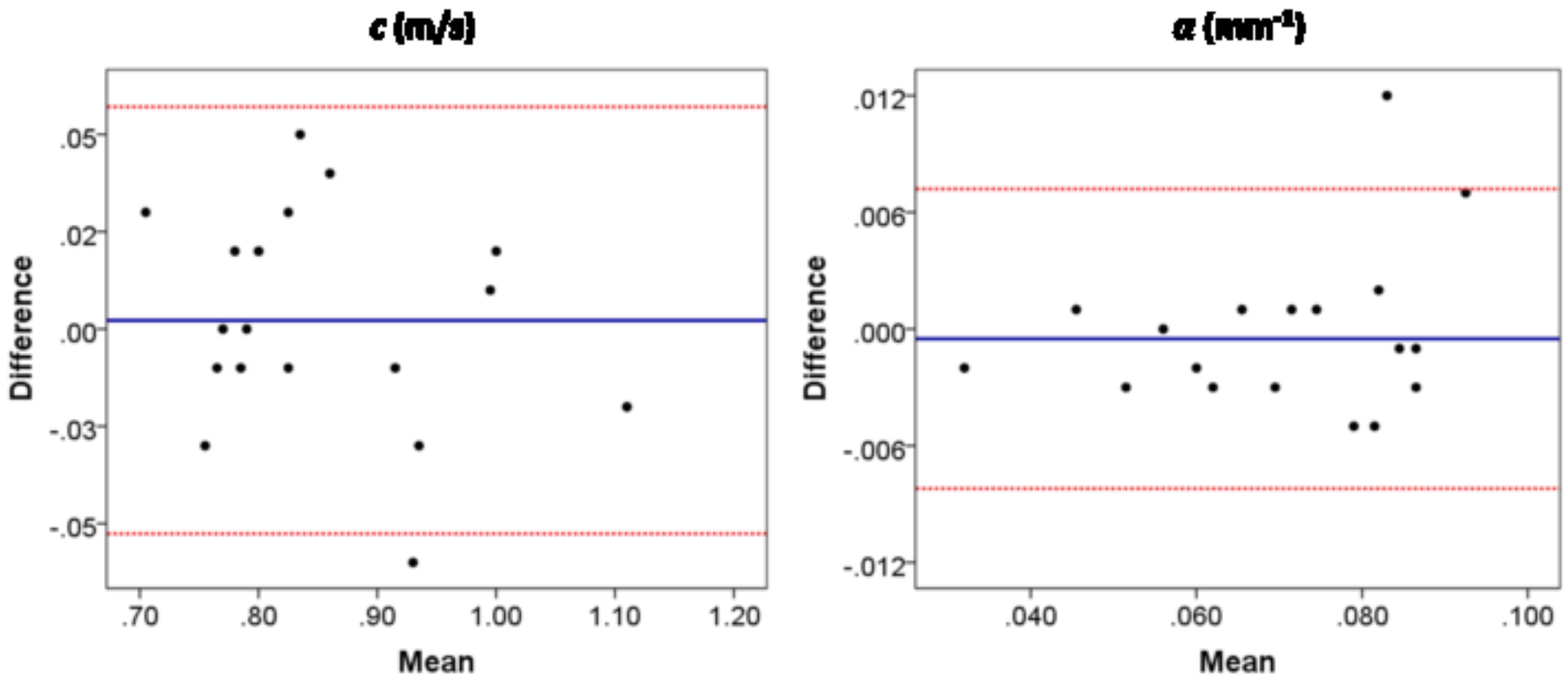

Figure 4

Click here to download Figure Figure 4.png

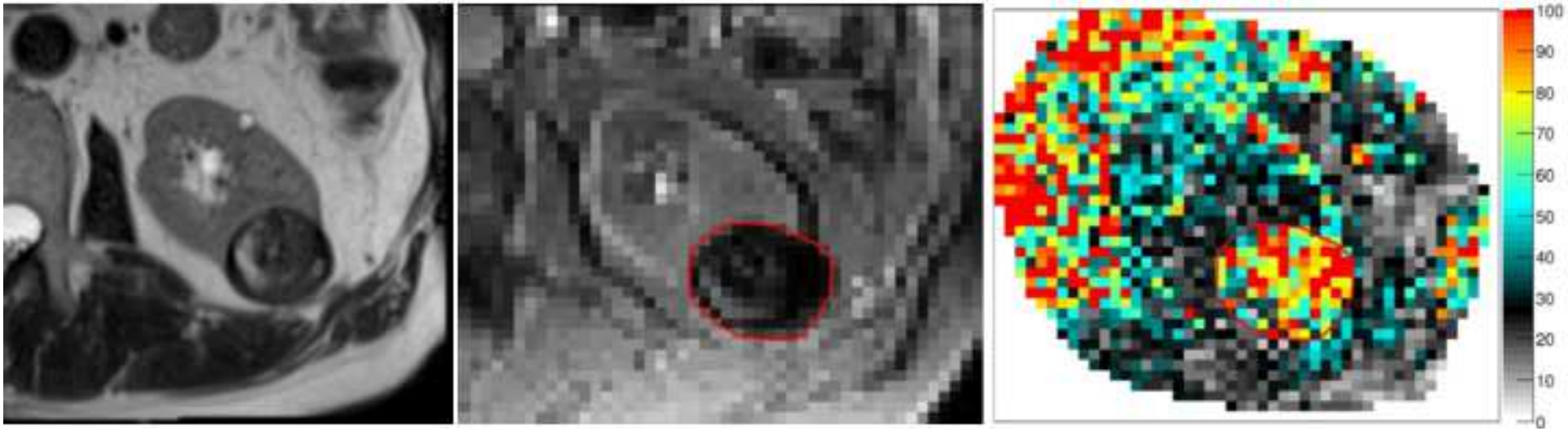

Title

Characterization of Small Renal Tumors with MR Elastography: a Feasibility Study

Abstract

Objectives

To explore the feasibility of magnetic resonance elastography (MRE) for characterizing indeterminate small renal tumors (SRT) as part of a multiparametric MR imaging protocol.

Materials and Methods

Following institutional review board approval and informed consent, 21 prospective adults (15 men, median age 55 [range 25-72] years) with SRT were enrolled. Tumors (2 – 5 cm Ø) were imaged using three-directional, gradient echo MRE. Viscoelastic parametric maps (shear wave velocity [*c*] and attenuation [α]) were analyzed by two independent radiologists. Interobserver agreement (Bland-Altman statistics and intraclass correlation coefficients [ICC]) was assessed. Anatomical T2-weighted, dynamic contrast enhanced (DCE) and diffusion sequences completed the acquisition protocol. Imaging parameters were compared between groups (Mann-Whitney U test).

Results

MRE quality was good in 18 cases (mean non-linearity <50%), including one papillary renal cell carcinoma and one metanephric adenoma. A cohort of 5 oncocytomas and 11 clear-cell renal cell carcinomas (ccRCC) was analyzed for statistical differences. MRE viscoelastic parameters were the strongest imaging discriminators: oncocytomas displayed significantly

lower shear velocity *c* (median, 0.77 m/s; interquartile range [IQR], 0.76-0.79) (*P* = 0.007) and higher shear attenuation α (median, 0.087 mm^{-1}; IQR, 0.082-0.087) (*P* = 0.008) than ccRCC (medians, 0.92 m/s and 0.066 mm^{-1}; IQR, 0.84-0.97 and 0.054-0.074 respectively). T2 signal intensity ratio (tumor/renal cortex) was lower in oncocytomas (*P* = 0.02). DCE and diffusion MR parameters overlapped substantially ($P \geq 0.1$). Oncocytomas displayed a consistent MRE viscoelastic profile, corresponding to data point clustering in a bidimensional scatter plot. MRE ICC were 0.982 for *c* and 0.984 for α, indicating excellent interobserver agreement.

Conclusions

MRE is feasible for SRT characterization; MRE viscoelastic parameters were stronger discriminators between oncocytoma and ccRCC than anatomical, DCE and diffusion MR imaging parameters.

Introduction

Small indeterminate renal tumors (SRT), defined as solid enhancing renal lesions measuring up to 4 cm in diameter, pose a growing challenge to clinical practice (1, 2). Renal cell carcinoma (RCC) accounts for the majority of cases but up to 20% of SRT are benign (3). A recent estimate suggests that ~5600 benign renal tumors undergo surgical resection yearly in the US (4). Image-guided biopsy is performed increasingly to confirm the diagnosis preoperatively (5). Despite providing excellent concordance with surgical histology (6), biopsy is invasive and non-diagnostic in up to 20% of cases (7). A reliable, non-invasive imaging strategy to distinguish benign from malignant SRT would be advantageous, mostly so in patients with multiple comorbidities, and potentially cost effective.

Anatomical and functional MR imaging parameters have shown potential individually to discriminate benign SRT from specific types of RCC (8-16), but their combined diagnostic accuracy has not been investigated in a prospective series to date. Oncocytoma and solid clear cell RCC (ccRCC), respectively the most common benign and malignant indeterminate SRT, share structural and physiological traits (high water content, prominent stroma, dense vascularity) that make their distinction by anatomical and functional MR imaging challenging in many cases (11, 12).

Yet their pathological gross appearance and microscopic structure clearly differ (17, 18): oncocytomas are typically homogenous lesions with frequent central scarring and absent necrosis; microscopically, they are composed of tight cellular nests surrounded by myxoid stroma. Clear cell RCC have a variegated appearance consisting of soft yellow material alternating with areas of hemorrhage, fibrosis, necrosis and cystic degeneration; microscopically, they are composed of lipid- and glycogen-rich cells surrounded by an

extensive capillary network. Oncocytomas have no recognized malignant transformation potential and, once diagnosed, conservative management is safe (19).

MR Elastography (MRE) is an emerging technique that evaluates soft tissue's viscoelastic properties by measuring the shear waves produced by a vibrating mechanical transducer (20). It has been readily incorporated into clinical MR imaging protocols and has been employed successfully in the assessment of hepatic fibrosis (21, 22) and for lesion characterization in the liver, central nervous system and breast (23-26).

We hypothesized that the viscoelastic shear properties of SRT measured by MRE would reflect the underlying tumor composition (e.g. cellular density, extracellular collagen, hemorrhage, necrosis) and architecture (e.g. cellular and connective tissue distribution, vascular size, density and permeability) and therefore differ between histopathological groups. In this study, we aimed to explore the feasibility and diagnostic potential of MRE, performed as part of a multiparametric MR imaging protocol, for characterizing indeterminate small renal tumors (SRT) in patients scheduled for surgery.

Materials and Methods

Participants

This prospective feasibility study was conducted between August 2015 and October 2016, following approval by the national research ethics committees; informed written consent was obtained from all subjects.

Twenty-one patients (15 men and 6 women) with a median age of 55 years (range, 25 to 72 years) and median BMI of 27.0 (range, 19.0 to 29.4), were recruited from a tertiary-care urological clinic. Patients were potentially eligible if under consideration for surgical

resection (partial or total nephrectomy) of an indeterminate solid renal mass measuring ≤5 cm in maximum diameter on cross-sectional imaging. Exclusion criteria were standard contraindications to contrast enhanced MR imaging (e.g. cardiac pacemaker, cochlear implant, significant renal impairment i.e. eGFR <50 mL/min or serum creatinine > 180 μmol/L).

MR Imaging Acquisition

MR imaging was performed on a 3.0 Tesla system (Biograph mMR, Siemens Healthcare GmbH, Erlangen, Germany). The protocol included MRE, anatomical T1 and T2 weighted sequences, dynamic contrast enhanced (DCE) MRI and diffusion-weighted imaging. Patients lied supine (head first) in the scanner and fasted for 4 hours before imaging.

MRE Acquisition

Mechanical vibrations were generated at a frequency of 30 Hz and at 70% of the maximum power by a remote loudspeaker (Resoundant®) and transmitted via compressed air to a disc-shaped passive transducer applied over the patient's flank of interest (mid-axillary line, held in place by an elastic band). A frequency of 30 Hz was selected as a compromise between resolution and efficient wave penetration in the retroperitoneum. MRE was based upon a prototype 2D multi-slice interleaved gradient echo sequence synchronized with the transducer's vibrations (27): repetition time, 11.11 ms (3 shots with a vibration frequency of 30Hz, corresponding to a period of 33.33 ms); echo time, 7.38 ms; motion encoding gradient amplitude, 30 mT/m; GRAPPA parallel imaging acceleration factor, 2; FOV, 265 x 385 mm. Four acquisitions in consecutive expiratory breath holds of 17 s (corresponding to 3 motion-encoding directions and one reference measurement without motion encoding) provided

MRE data within 6 consecutive slices of 128 x 88 pixels at 3 mm isotropic resolution and 4 wave phase offsets. Measurements were performed at mid-tumor level and repeated in 1 or 2 normal portions of the same kidney (standardized to either upper pole, mid-kidney or lower pole), in order to obtain reference measurements from healthy renal parenchyma. Each MRE measurement had an approximate duration of 2 minutes.

MRE Reconstruction

MRE reconstruction used firstly the application of the curl operator for removal of the compressional component, secondly a direct inversion of the Helmholtz equation (28). Parametric maps of shear wave velocity (*c*), a measure of tissue elasticity, and attenuation (α), a measure of viscosity, were generated offline using dedicated in-house software, validated previously (28-30).

Data post-processing was performed by a physicist with over 20 years of experience in MRE. Tumor data analysis was performed independently by two board-certified radiologists with over 7 years of experience in abdominal MR imaging (MRE observer 1 and 2), blinded to histopathology results. Normal kidney measurements were performed by a single radiologist (MRE observer 1).

Free-hand regions of interest (ROI) were drawn around each tumor and around normal renal parenchyma (including both cortex and medulla, aiming to match the size of tumor ROI) on the two contiguous central slices of magnitude images, with reference to the available anatomical sequences, and copied onto the parametric maps. The mean and standard deviation of the quantified parameters were recorded for each case.

MRE Quality Assessment

Parametric maps of data 'non-linearity', displaying the percentage deviation of the phase signal from a perfect sinusoidal modulation, were assessed by both readers for each MRE measurement, using the same ROI as previously, and the mean 'non-linearity' percentage documented. A threshold of <50% mean 'non-linearity' was defined as acceptable data quality.

Anatomical and Functional MR Imaging

Anatomical imaging included a T2-weighted half-Fourier single-shot turbo spin echo sequence (HASTE) (TR, 1000 msec; TE, 97 msec; FA, 135°; NEX, 1; GRAPPA parallel imaging acceleration factor, 2; FOV, 384 x 250 mm; pixel size, 1.5 x 1.2 x 3.0 mm) acquired in the axial plane.

Dynamic contrast-enhanced (DCE) MR imaging was based on a 3D T1-weighted axial volumetric interpolated spoiled gradient echo sequence (VIBE) (TR, 4.62 msec; TE, 1.72 msec; FA, 18°; number of signals acquired, 1; parallel imaging acceleration factor, 2; FOV, 300 x 244 mm; pixel size, 1.8 x 1.3 x 4.0 mm). 0.1 mmol/kg of gadolinium contrast agent was administered intravenously (Gadovist®, Bayer) at a rate of 4 mL/sec using a power injector, followed by a 20 mL saline chaser; 30 volumes were acquired post contrast injection over 3 minutes, resulting in a temporal resolution of 6.4 sec. The dynamic acquisition was preceded by a T1 calibration sequence with the same parameters except a flip angle of 3°.

Diffusion-weighted imaging consisted of free-breathing single-shot echo-planar imaging in the axial plane with *b* values of 50, 500 and 800 mm^2/sec. Imaging parameters were as follows: TR, 6100 msec; TE, 62 msec; NEX, 5; parallel imaging acceleration factor, 2; FOV, 380 x 285 mm; pixel size 3.7 x 3.0 x 4.0 mm.

Anatomical and functional sequences were post processed and analyzed offline on a commercial platform (Multimodality Workplace, Siemens). All quantitative measurements were performed by a single radiologist (MRE observer 1), blinded to histopathology. Freehand ROI were drawn on each slice displaying the lesion of interest; volumetric means were analyzed. T2 signal intensity (SI) ratio was calculated as the % ratio of tumor over renal cortex on the T2 HASTE sequence (8).

DCE MR imaging parametric maps, including transfer coefficient (K^{trans}), rate constant (k_{ep}), extracellular-extravascular space fractional volume (v_e) and initial area under the concentration curve for the first 60 seconds ($iAUC_{60}$), were generated on dedicated software (Tissue 4D; Siemens); nonrigid motion correction and registration to the calibration sequence were applied to the dynamic acquisition; quantification was based on the two-compartment Tofts model (31), using a pre-set population averaged arterial input function. Apparent diffusion coefficient (ADC) maps were generated by fitting a mono-exponential function to all *b* values.

Statistics

All statistical analyses were performed using IBM SPSS version 23.0 software. Continuous variables were regarded as non-normally distributed and expressed as medians and interquartile range. Measurements were compared between the two main histological groups using the non-parametric Mann-Whitney U test. Mean interobserver MRE values were used in the analysis. $P < .05$ was considered indicative of a significant difference. Interobserver agreement was assessed using Bland-Altman (BA) statistics and intraclass correlation coefficients (ICC). MRE within-subject variability in healthy renal parenchyma

was expressed in terms of mean differences and coefficients of variance (CV). Missing data were omitted from the analysis.

Results

One patient did not complete imaging due to claustrophobia, leaving 20 complete imaging datasets including MRE. Surgical histopathology became available for 19 patients and revealed 4 renal oncocytomas, 12 ccRCC (1, Fuhrman grade 3; 8, grade 2; 3, grade 1), 2 papillary RCC and 1 metanephric adenoma. One further case of renal oncocytoma was diagnosed from image-guided biopsy and surgery was deferred. Tumor diameters ranged between 2.2 and 5.0 cm. All imaging sessions were completed in less than 60 minutes.

MRE of Tumors

Two tumor MRE datasets were excluded for insufficient quality, secondary to poor patient compliance with breath hold instructions and consequent high data non-linearity (>50%), leaving a cohort of 11 clear cell renal cell carcinomas (ccRCC) and 5 oncocytomas for statistical analysis.

Shear wave velocity *c* was significantly lower in oncocytomas (median, 0.77 m/s; interquartile range (IQR), 0.76-0.79) than in ccRCC (median, 0.92 m/s; IQR, 0.84-0.97) (P = 0.007). Shear wave attenuation α was significantly higher in oncocytomas (median, 0.087 mm^{-1}; IQR, 0.082-0.087) than in ccRCC (median, 0.066 mm^{-1}; IQR, 0.054-0.074) (P = 0.008). Complete results, including case-by-case mean values and standard deviations, are reported in Table 1. Pictorial examples are shown in Figure 1. Oncocytomas displayed a relatively narrow range of values (*c* range, 0.71-0.83 m/s; α range, 0.082-0.093 mm^{-1}), corresponding

to data point clustering in a bidimensional scatter plot (Figure 2). ccRCC had wider ranges (*c* range, 0.79-1.11 m/s; α range, 0.046-0.083 mm^{-1}), resulting in a broader data point scatter. The only papillary RCC imaged with sufficient data quality showed relatively low *c* (0.77 m/s, coinciding with the median value of oncocytomas) and low α (0.064 mm^{-1}, close to the median of ccRCC). Metanephric adenoma displayed relatively low *c* (0.78 m/s) and intermediate α (0.079 mm^{-1}).

MRE Interobserver Agreement

Mean ROI size was 226 ± 109 pixels for observer 1 and 196 ± 102 pixels for observer 2. Mean differences in tumors were 0.002 m/s [*c*] and -0.0005 mm^{-1} [α]. Bland-Altman limits of agreement were the mean differences as previously ± 0.055 m/s [*c*] and ± 0.0077 mm^{-1} [α] respectively (Figure 3). ICC (95% confidence intervals) were 0.982 (0.953-0.993) [*c*] and 0.984 (0.957-0.994) [α], indicating excellent agreement.

MRE of Normal Kidney

A total of 31 MRE measurements of acceptable quality were performed in normal portions of the tumor-containing kidneys. Mean shear velocity *c* in the renal parenchyma was 0.89 ± 0.10 m/s; mean shear attenuation α was 0.072 ± 0.012 mm^{-1}.

Two separate measurements in different portions of the same kidney were acquired in a subset of 10 patients. Mean within-subject differences were 0.10 ± 0.05 m/s for *c* and 0.014 ± 0.010 mm^{-1} for α, corresponding to CV of 7.81 ± 4.61% and 14.24 ± 10.72% respectively.

Anatomical and Functional MR Imaging of Tumors

Tumor parametric values are reported in Table 1. Oncocytomas had significantly lower T2 SI ratio (median, 93%; interquartile range, 89-93%) than ccRCC (median, 120%; interquartile

range, 103-128%) (P = 0.020). No statistically significant difference between the two histological groups was observed among functional MR imaging parameters. Oncocytomas appeared on average more vascular on DCE MR imaging, with higher $iAUC_{60}$ (median, 59 mmol; P = 0.100), K^{trans} (median, 0.24 min^{-1}; P = 0.126), k_{ep} (median, 0.66 min^{-1}; P = 0.193) and lower v_e (median, 0.30 mL/100 mL; P = 0.692). ADC varied considerably within both groups, being on average lower in oncocytomas (median, 1363 x 10^{-6} mm^2/s) (P = 0.193). Both papillary RCC displayed markedly restricted diffusion (ADC = 839 and 959 x 10^{-6} mm^2/s) and low T2 SI ratios (74% and 55%), in line with the existing literature (32, 33). The metanephric adenoma showed relatively low T2 SI ratio (58%) and contrast enhancement ($iAUC_{60}$ = 19 mmol)(34). Only partial data point clustering was obtained by plotting T2 SI ratio against ADC (Figure 2B). No clustering was observed by plotting DCE MR K^{trans} against v_e (Figure 2C).

Among qualitative anatomical tumor features, a T2 pseudocapsule was present in 2 out of 5 oncocytomas and 10 out of 12 ccRCC; central T2 hyperintensity was observed in 3 oncocytomas and 1 ccRCC; and signal drop on opposed-phase chemical shift MRI in no oncocytoma and 7 ccRCC.

Discussion

Our study shows that MRE is feasible, as part of a multiparametric MR protocol, for the characterization of small indeterminate renal tumors and represents a promising technique for distinguishing benign oncocytoma from malignant clear cell carcinoma. MRE shear velocity *c* and shear attenuation α were the strongest imaging discriminators between oncocytoma and ccRCC in this initial prospective cohort of 20 patients.

Identifying renal oncocytoma among indeterminate SRT is problematic based on imaging alone, even using multiparametric MR, as highlighted by current literature. Among anatomical MR imaging parameters, T2 signal intensity has been shown to be higher in ccRCC than in oncocytoma and chromophobe RCC, but the overlap is substantial (35, 36). T2 SI ratio was in fact the third best discriminator between oncocytoma and ccRCC in our study. The presence of a central area of T2 signal hyperintensity, compatible with necrosis or fibrosis, can be observed in both oncocytoma and RCC (8, 9). Chemical shift MR, combined with delayed contrast enhanced imaging, has been found to have a high negative predictive value for oncocytoma (97%), by revealing the typical absence of fat and the presence of enhancing central fibrosis: these findings, however, have yet to be validated prospectively (10). A T2 hypointense pseudocapsule, commonly observed in SRT, is also nonspecific (16). Diffusion and contrast enhancement characteristics can discriminate between types of RCC but again are known to overlap between oncocytoma and ccRCC (32, 37); this was the case in our cohort, where DCE MR $iAUC_{60}$ was the strongest functional discriminator (P = .10), being higher in oncocytomas. Taouli et al. previously found significantly lower ADC values in solid ccRCC than in oncocytomas, but only after excluding Bosniak 4 ccRCC (i.e. solid masses with a large cystic or a necrotic component), potentially indistinguishable from oncocytoma in our experience (11). No significant signal intensity change was observed by Vargas et al. on contrast-enhanced MR between ccRCC and oncocytoma in any phase of enhancement (12).

To our knowledge, this study is the first to investigate the viscoelastic properties of SRT using MRE. Published reports employing semiquantitative (strain) or quantitative (shear-wave) ultrasound elastography techniques for differentiating benign from malignant renal

tumors found RCC to be stiffer than benign lesions such as angiomyolipoma; no oncocytomas were included, however (38-40).

Our results support the hypothesis that differences in tumor composition and structural architecture, clearly distinguishable on histopathology between oncocytoma and RCC, are reflected by MRE viscoelastic shear properties. Oncocytomas showed lower shear wave velocity, corresponding to lower stiffness (storage modulus), and higher shear attenuation (loss modulus), corresponding to higher viscosity, than ccRCC. This is in line with the evidence that malignancy increases stiffness through collagen deposition in the extracellular matrix and raised interstitial pressure levels from the altered vasculature (41, 42). Lower MRE stiffness values in benign versus malignant tumors have been documented in the breast and in the liver (23, 26, 43, 44).

Few studies to date have assessed tumors in terms of shear wave attenuation. The loss modulus was found to be significantly higher in hepatocellular carcinoma than in benign liver tumors (hemangioma, focal nodular hyperplasia, adenoma) by Garteiser et al. (23), contrasting with our results. We speculate that the higher shear wave attenuation values measured in oncocytoma might reflect a high density of capillaries with normal endothelium, resulting in efficient energy dispersion in the form of heat and contrasting with the disorganized vasculature and leaky endothelium typical of renal carcinomas.

Propagating waves could be appreciated on phase images in all MRE acquisitions. Two out of 20 datasets were excluded for insufficient quality, defined as nonlinearity >50%. In one case (ccRCC-07, Table 1), respiratory motion was identified as the main causative factor from the presence of blurred renal contours on the magnitude images. In the second case (papRCC-02) (Figure 4), wave penetration inside the lesion was inconsistent with an incompressible material (as if detached from the surrounding tissue) despite good

penetration in the adjacent kidney; this was a hemorrhagic papillary RCC showing marked signal hypointensity on T2 HASTE. Interestingly, one of the main causes identified by Wagner et al. for technical MRE failure in the liver at 3T (45) was hepatic iron deposition, causing shortening of T2* relaxation. Intratumoral hemorrhage is frequent in papillary RCC, but is not known to occur in oncocytoma; low ADC values are the dominant MR feature of papillary RCC and in our experience it seems unlikely that MRE will be the main determinant for papillary RCC characterization.

The average level of phase signal nonlinearity was ~30% throughout MRE acquisitions, corresponding to our previous clinical experience using the Resoundant® system in the upper abdomen. New bespoke transducers, based upon a gravitational concept for generating shear waves (46), are expected to lower this level and thereby increase the reproducibility of viscoelastic parameters. MRE interobserver limits of agreement (mean difference ± 0.055 m/s [*c*] and ± 0.0077 mm^{-1} [α]) were deemed within acceptable limits and appear unlikely to affect the significance of between-group differences.

Of the two MRE parameters, *c* was less dispersed around the mean value in tumor ROI: SD ranged between 0.11 and 0.30 m/s (Table 1), corresponding to a CV of ~14-28%. MRE *c* SD were noticeably lower in oncocytomas than ccRCC; this was not the case for MRE α or anatomical/functional MR imaging parameters. Within-subject variability in healthy renal parenchyma was 7.81 ± 4.61% for *c* and 14.24 ± 10.72% for α. Similarly, Rouviere et al. (47) found a mean shear wave velocity variation of 6% (range, 2 - 16%) between two independent measurements in the kidney of young healthy adults at 45 Hz, also using a gradient echo sequence at 1.5 T. Although not directly comparable, a recent meta-analysis on MRE repeatability in the liver identified a measured change in hepatic stiffness of 22% or greater as a reliable true change (95% confidence) (48).

Despite our promising results, our study does have limitations: the small study cohort reflects its exploratory nature and does not allow us to draw definitive conclusions on the diagnostic accuracy of MR imaging parameters. Prospective recruitment of consecutive patients from a single tertiary clinic meant that only the most common SRT histologies were captured. The decision to include tumors ≤ 5 cm in diameter (contrasting with the conventional definition of small renal mass, ≤ 4 cm) was made to facilitate patient recruitment. Less common histologies such as chromophobe RCC, often morphologically indistinguishable from oncocytoma (36), and fat poor AML (35) were not part of our prospective cohort.

In conclusion, MRE is feasible and practicable for the characterization of small indeterminate renal tumors as part of a multiparametric MR protocol. This feasibility study highlights the diagnostic potential of MRE for distinguishing renal oncocytoma from ccRCC, strengthening the case for confirmation of these results in a powered diagnostic accuracy study.

References

1. Hollingsworth JM, Miller DC, Daignault S, Hollenbeck BK. Rising incidence of small renal masses: a need to reassess treatment effect. J Natl Cancer Inst. 2006;98(18):1331-4.

2. Gill IS, Aron M, Gervais DA, Jewett MA. Clinical practice. Small renal mass. N Engl J Med. 2010;362(7):624-34.

3. Frank I, Blute ML, Cheville JC, Lohse CM, Weaver AL, Zincke H. Solid renal tumors: an analysis of pathological features related to tumor size. J Urol. 2003;170(6 Pt 1):2217-20.

4. Johnson DC, Vukina J, Smith AB, et al. Preoperatively misclassified, surgically removed benign renal masses: a systematic review of surgical series and United States population level burden estimate. J Urol. 2015;193(1):30-5.

5. Finelli A, Ismaila N, Russo P. Management of Small Renal Masses: American Society of Clinical Oncology Clinical Practice Guideline Summary. J Oncol Pract. 2017:JOP2016019620.

6. Marconi L, Dabestani S, Lam TB, et al. Systematic Review and Meta-analysis of Diagnostic Accuracy of Percutaneous Renal Tumour Biopsy. Eur Urol. 2016;69(4):660-73.

7. Leveridge MJ, Finelli A, Kachura JR, et al. Outcomes of small renal mass needle core biopsy, nondiagnostic percutaneous biopsy, and the role of repeat biopsy. Eur Urol. 2011;60(3):578-84.

8. Rosenkrantz AB, Hindman N, Fitzgerald EF, Niver BE, Melamed J, Babb JS. MRI features of renal oncocytoma and chromophobe renal cell carcinoma. AJR Am J Roentgenol. 2010;195(6):W421-7.

9. Ball DS, Friedman AC, Hartman DS, Radecki PD, Caroline DF. Scar sign of renal oncocytoma: magnetic resonance imaging appearance and lack of specificity. Urol Radiol. 1986;8(1):46-8.

10. Cornelis F, Lasserre AS, Tourdias T, et al. Combined late gadolinium-enhanced and double-echo chemical-shift MRI help to differentiate renal oncocytomas with high central T2 signal intensity from renal cell carcinomas. AJR Am J Roentgenol. 2013;200(4):830-8.

11. Taouli B, Thakur RK, Mannelli L, et al. Renal lesions: characterization with diffusion-weighted imaging versus contrast-enhanced MR imaging. Radiology. 2009;251(2):398-407.

12. Vargas HA, Chaim J, Lefkowitz RA, et al. Renal cortical tumors: use of multiphasic contrast-enhanced MR imaging to differentiate benign and malignant histologic subtypes. Radiology. 2012;264(3):779-88.

13. Kang SK, Zhang A, Pandharipande PV, Chandarana H, Braithwaite RS, Littenberg B. DWI for Renal Mass Characterization: Systematic Review and Meta-Analysis of Diagnostic Test Performance. AJR Am J Roentgenol. 2015;205(2):317-24.

14. Sasiwimonphan K, Takahashi N, Leibovich BC, Carter RE, Atwell TD, Kawashima A. Small (<4 cm) renal mass: differentiation of angiomyolipoma without visible fat from renal cell carcinoma utilizing MR imaging. Radiology. 2012;263(1):160-8.

15. Verma SK, Mitchell DG, Yang R, et al. Exophytic renal masses: angular interface with renal parenchyma for distinguishing benign from malignant lesions at MR imaging. Radiology. 2010;255(2):501-7.

16. Roy C, El Ghali S, Buy X, et al. Significance of the pseudocapsule on MRI of renal neoplasms and its potential application for local staging: a retrospective study. AJR Am J Roentgenol. 2005;184(1):113-20.

17. Amin MB, Crotty TB, Tickoo SK, Farrow GM. Renal oncocytoma: a reappraisal of morphologic features with clinicopathologic findings in 80 cases. Am J Surg Pathol. 1997;21(1):1-12.

18. Andeen N. Kidney tumor - cysts, children, adult benign. Adult renal cell carcinoma. Clear cell renal cell carcinoma. http://www.pathologyoutlines.com/topic/kidneytumormalignantrccclear.html. Published January 30, 2017. Accessed September 4, 2017.

19. Romis L, Cindolo L, Patard JJ, et al. Frequency, clinical presentation and evolution of renal oncocytomas: multicentric experience from a European database. Eur Urol. 2004;45(1):53-7; discussion 7.

20. Muthupillai R, Lomas DJ, Rossman PJ, Greenleaf JF, Manduca A, Ehman RL. Magnetic resonance elastography by direct visualization of propagating acoustic strain waves. Science. 1995;269(5232):1854-7.

21. Bohte AE, Garteiser P, De Niet A, et al. MR elastography of the liver: defining thresholds for detecting viscoelastic changes. Radiology. 2013;269(3):768-76.

22. Singh S, Venkatesh SK, Wang Z, et al. Diagnostic performance of magnetic resonance elastography in staging liver fibrosis: a systematic review and meta-analysis of individual participant data. Clin Gastroenterol Hepatol. 2015;13(3):440-51.e6.

23. Garteiser P, Doblas S, Daire JL, et al. MR elastography of liver tumours: value of viscoelastic properties for tumour characterisation. Eur Radiol. 2012;22(10):2169-77.

24. Hughes JD, Fattahi N, Van Gompel J, et al. Higher-Resolution Magnetic Resonance Elastography in Meningiomas to Determine Intratumoral Consistency. Neurosurgery. 2015;77(4):653-8; discussion 8-9.

25. Hughes JD, Fattahi N, Van Gompel J, Arani A, Ehman R, Huston J. Magnetic resonance elastography detects tumoral consistency in pituitary macroadenomas. Pituitary. 2016;19(3):286-92.

26. Sinkus R, Tanter M, Xydeas T, Catheline S, Bercoff J, Fink M. Viscoelastic shear properties of in vivo breast lesions measured by MR elastography. Magn Reson Imaging. 2005;23(2):159-65.

27. Garteiser P, Sahebjavaher RS, Ter Beek LC, et al. Rapid acquisition of multifrequency, multislice and multidirectional MR elastography data with a fractionally encoded gradient echo sequence. NMR Biomed. 2013;26(10):1326-35.

28. Sinkus R, Siegmann K, Xydeas T, Tanter M, Claussen C, Fink M. MR elastography of breast lesions: understanding the solid/liquid duality can improve the specificity of contrast-enhanced MR mammography. Magn Reson Med. 2007;58(6):1135-44.

29. Green MA, Bilston LE, Sinkus R. In vivo brain viscoelastic properties measured by magnetic resonance elastography. NMR Biomed. 2008;21(7):755-64.

30. Etchell E, Jugé L, Hatt A, Sinkus R, Bilston LE. Liver Stiffness Values Are Lower in Pediatric Subjects than in Adults and Increase with Age: A Multifrequency MR Elastography Study. Radiology. 2017;283(1):222-30.

31. Tofts PS, Kermode AG. Measurement of the blood-brain barrier permeability and leakage space using dynamic MR imaging. 1. Fundamental concepts. Magn Reson Med. 1991;17(2):357-67.

32. Wang H, Cheng L, Zhang X, et al. Renal cell carcinoma: diffusion-weighted MR imaging for subtype differentiation at 3.0 T. Radiology. 2010;257(1):135-43.

33. Oliva MR, Glickman JN, Zou KH, et al. Renal cell carcinoma: t1 and t2 signal intensity characteristics of papillary and clear cell types correlated with pathology. AJR Am J Roentgenol. 2009;192(6):1524-30.

34. Yan J, Cheng JL, Li CF, et al. The findings of CT and MRI in patients with metanephric adenoma. Diagn Pathol. 2016;11(1):104.

35. Schieda N, Dilauro M, Moosavi B, et al. MRI evaluation of small (<4cm) solid renal masses: multivariate modeling improves diagnostic accuracy for angiomyolipoma without visible fat compared to univariate analysis. Eur Radiol. 2016;26(7):2242-51.

36. Galmiche C, Bernhard JC, Yacoub M, Ravaud A, Grenier N, Cornelis F. Is Multiparametric MRI Useful for Differentiating Oncocytomas From Chromophobe Renal Cell Carcinomas? AJR Am J Roentgenol. 2017;208(2):343-50.

37. Wang HY, Su ZH, Xu X, et al. Dynamic Contrast-enhanced MRI in Renal Tumors: Common Subtype Differentiation using Pharmacokinetics. Sci Rep. 2017;7(1):3117.

38. Tan S, Özcan MF, Tezcan F, et al. Real-time elastography for distinguishing angiomyolipoma from renal cell carcinoma: preliminary observations. AJR Am J Roentgenol. 2013;200(4):W369-75.

39. Göya C, Daggulli M, Hamidi C, et al. The role of quantitative measurement by acoustic radiation force impulse imaging in differentiating benign renal lesions from malignant renal tumours. Radiol Med. 2015;120(3):296-303.

40. Lu Q, Wen JX, Huang BJ, Xue LY, Wang WP. Virtual Touch quantification using acoustic radiation force impulse (ARFI) technology for the evaluation of focal solid renal lesions: preliminary findings. Clin Radiol. 2015;70(12):1376-81.

41. Dvorak HF. Tumors: wounds that do not heal. Similarities between tumor stroma generation and wound healing. N Engl J Med. 1986;315(26):1650-9.

42. Heldin CH, Rubin K, Pietras K, Ostman A. High interstitial fluid pressure - an obstacle in cancer therapy. Nat Rev Cancer. 2004;4(10):806-13.

43. Hennedige TP, Hallinan JT, Leung FP, et al. Comparison of magnetic resonance elastography and diffusion-weighted imaging for differentiating benign and malignant liver lesions. Eur Radiol. 2016;26(2):398-406.

44. McKnight AL, Kugel JL, Rossman PJ, Manduca A, Hartmann LC, Ehman RL. MR elastography of breast cancer: preliminary results. AJR Am J Roentgenol. 2002;178(6):1411-7.

45. Wagner M, Corcuera-Solano I, Lo G, et al. Technical Failure of MR Elastography Examinations of the Liver: Experience from a Large Single-Center Study. Radiology. 2017:160863.

46. Runge J, Hoelzl S, Sudakova J, et al. A novel MR Elastography transducer concept based on a rotational eccentric mass: the gravitational transducer. Conference abstract #1369. ISMRM Annual Meeting 2017, Honolulu, USA.

47. Rouvière O, Souchon R, Pagnoux G, Ménager JM, Chapelon JY. Magnetic resonance elastography of the kidneys: feasibility and reproducibility in young healthy adults. J Magn Reson Imaging. 2011;34(4):880-6.

48. Serai SD, Obuchowski NA, Venkatesh SK, et al. Repeatability of MR Elastography of Liver: A Meta-Analysis. Radiology. 2017:161398.

Tables

Table 1. Results from tumor multiparametric MR imaging, displayed by tumor histology.

Note. Tumor diameters as measured at surgical histopathology. Mean values ± standard deviation. *P* values for between-group comparisons were determined with the Mann-Whitney U test. IQR = interquartile range. - = missing value.

Case #	Diameter (cm)	*c* (m/s)	α (mm^{-1})	$iAUC_{60}$ (mmol)	K^{trans} (min^{-1})	K_{ep} (min^{-1})	V_e (mL/100 mL)	T2 SI RATIO (%)	ADC (10^{-6} x mm^2/s)
RENAL ONCOCYTOMA									
ONCO-1	4.2	0.83 ± 0.16	0.093 ± 0.033	72 ± 34	0.31 ± 0.17	0.99 ± 0.37	0.30 ± 0.14	93 ± 30	1949 ± 338
ONCO-2	5.0	0.79 ± 0.16	0.082 ± 0.035	32 ± 16	0.09 ± 0.05	0.32 ± 0.16	0.28 ± 0.15	86 ± 27	1319 ± 260
ONCO-3	5.0	0.77 ± 0.14	0.082 ± 0.048	80 ± 38	0.41 ± 0.24	1.15 ± 0.58	0.33 ± 0.17	89 ± 24	1348 ± 284
ONCO-4	3.1	0.76 ± 0.11	0.087 ± 0.044	59 ± 22	0.24 ± 0.10	0.62 ± 0.23	0.39 ± 0.14	124 ± 40	1961 ± 315
ONCO-5	4.5	0.71 ± 0.11	0.087 ± 0.042	51 ± 32	0.20 ± 0.13	0.66 ± 0.26	0.29 ± 0.16	93 ± 30	1363 ± 231
Median (IQR)	4.5 (4.2-5.0)	0.77 (0.76-0.79)	0.087 (0.082-0.087)	59 (51-72)	0.24 (0.20-0.31)	0.66 (0.62-0.99)	0.30 (0.29-0.33)	93 (89-93)	1363 (1348-1949)
CLEAR CELL RENAL CELL CARCINOMA									
ccRCC-01	3.3	1.00 ± 0.28	0.060 ± 0.027	29 ± 20	0.11 ± 0.09	0.47 ± 0.30	0.24 ± 0.17	126 ± 40	1760 ± 326
ccRCC-02	3.0	0.79 ± 0.12	0.072 ± 0.054	63 ± 29	0.21 ± 0.10	0.51 ± 0.15	0.40 ± 0.17	106 ± 23	1590 ± 184
ccRCC-03	3.6	0.83 ± 0.16	0.070 ± 0.040	50 ± 43	0.19 ± 0.20	0.41 ± 0.36	0.33 ± 0.30	101 ± 34	1695 ± 365
ccRCC-04	2.8	0.94 ± 0.19	0.066 ± 0.035	55 ± 34	0.22 ± 0.17	0.74 ± 0.46	0.29 ± 0.17	102 ± 31	1722 ± 320
ccRCC-05	2.5	0.84 ± 0.23	0.083 ± 0.045	46 ± 32	0.17 ± 0.13	0.33 ± 0.23	0.45 ± 0.26	141 ± 44	2118 ± 394
ccRCC-06	3.0	0.86 ± 0.18	0.085 ± 0.030	23 ± 22	0.09 ± 0.09	0.63 ± 1.42	0.18 ± 0.17	121 ± 37	1929 ± 303
ccRCC-07	2.7	-	-	62 ± 44	0.24 ± 0.18	0.62 ± 0.38	0.33 ± 0.23	94 ± 32	1433 ± 255

ccRCC-08	3.5	1.11 ± 0.30	0.052 ± 0.032	27 ± 21	0.11 ± 0.09	0.30 ± 0.24	0.38 ± 0.27	152 ± 47	2483 ± 424
ccRCC-09	4.2	0.92 ± 0.24	0.046 ± 0.033	61 ± 31	0.27 ± 0.16	0.71 ± 0.28	0.37 ± 0.20	124 ± 45	1512 ± 460
ccRCC-10	4.0	0.93 ± 0.19	0.032 ± 0.022	47 ± 43	0.19 ± 0.18	0.68 ± 0.56	0.26 ± 0.24	104 ± 35	1795 ± 295
ccRCC-11	3.4	1.00 ± 0.23	0.075 ± 0.050	29 ± 21	0.11 ± 0.09	0.38 ± 0.38	0.30 ± 0.19	120 ± 54	1984 ± 348
ccRCC-12	2.2	0.80 ± 0.14	0.056 ± 0.028	51 ± 19	0.15 ± 0.07	0.30 ± 0.15	0.49 ± 0.22	134 ± 39	1612 ± 155
Median (IQR)	3.2 (2.8-3.5)	0.92 (0.84-0.97)	0.066 (0.054-0.074)	48 (29-57)	0.18 (0.11-0.21)	0.49 (0.36-0.64)	0.33 (0.28-0.39)	120 (103-128)	1741 (1606-1943)
***P* value**	.017	.007	.008	.100	.126	.193	.692	.020	.193
PAPILLARY RENAL CELL CARCINOMA									
papRCC-01	3.7	0.77 ± 0.10	0.062 ± 0.029	30 ± 20	0.11 ± 0.10	0.68 ± 0.40	0.17 ± 0.14	74 ± 17	839 ± 218
papRCC-02	4.1	-	-	15 ± 19	0.06 ± 0.04	0.50 ± 0.55	0.16 ± 0.10	55 ± 35	959 ± 602
METANEPHRIC ADENOMA									
MA-01	5.0	0.78 ± 0.15	0.079 ± 0.033	19 ± 12	0.11 ± 0.07	0.17 ± 0.20	0.37 ± 0.21	58 ± 14	1222 ± 339

Figure Captions

Figure 1. **A**. Fuhrman grade 2, 2.7 cm ccRCC in a 67-year-old man. **B**. 3.1 cm renal oncocytoma in a 51-year-old man. Axial MR imaging sections. Anatomical T2 HASTE (top left), ADC map (middle), cortico-medullary phase contrast-enhanced T1 VIBE (top right), MRE magnitude image (bottom left), MRE *c* (middle) and MRE α (bottom right) parametric maps. Morphological and functional imaging features are indistinguishable between the two histologies. Oncocytoma displays relatively lower shear velocity *c* and higher shear attenuation α. Tumors are contoured in red on MRE magnitude images and parametric maps. The adjacent kidney is contoured in pink and can be clearly distinguished from the surrounding structures on MRE shear velocity maps.

Figure 2. Bidimensional scatter plots of tumor MR imaging parameters. Oncocytomas display a consistent MRE viscoelastic profile, corresponding to data point clustering (A). Only partial clustering is obtained by plotting T2 SI ratio against ADC (B). No clustering is observed by plotting DCE MR K^{trans} against v_e (C).

Figure 3. Interobserver agreement. Bland-Altman graphs of MRE *c* (left) and α (right), plotting interobserver differences against their mean. Red dotted lines represent 95% Bland-Altman limits of agreement; blue line represents the mean difference.

Figure 4. Type 1, 4.1 cm papillary RCC in a 66-year-old man: axial MR imaging sections. Anatomical T2 HASTE (left), MRE gradient-echo magnitude image (middle) and MRE non-linearity parametric map (right). Intra-tumoral haemorrhage, confirmed at histology, corresponds to low signal intensity in A and B. MRE phase signal shows elevated non-linearity within the tumor (~80%) compared to adjacent renal parenchyma (~35%).